https://doi.org/10.5194/egusphere-2025-2498
Preprint. Discussion started: 18 July 2025

Fractal Characteristics of Ice-Supersaturated Regions in the Tropopause Region of the northern midlatitudes

Helena Schuh[1], Philipp Reutter[1], Stefan Niebler[2], and Peter Spichtinger[1]

[1]Institute for Atmospheric Physics, Johannes Gutenberg University Mainz, Mainz, Germany
[2]Institute for Computer Sciences, Johannes Gutenberg University Mainz, Mainz, Germany

Correspondence: Helena Schuh (hschuh01@students.uni-mainz.de)

Abstract. Ice supersaturated regions (ISSRs) are air masses in the upper troposphere and lower stratosphere (UTLS) where relative humidity with respect to ice (RHi) exceeds 100%, i.e. regions with enhanced water vapor concentrations. These are potential formation regions of cirrus clouds and contrails. While the impact of cloud free regions of enhanced water vapor on the planetary radiation balance is small to negligible, thin cirrus clouds and aircraft induced contrail cirrus formed within them might have a large radiative impact. Understanding the characteristics of ISSRs, including their geometry and seasonal variability, is essential for improving atmospheric models in representing ice clouds correctly. While ISSR's path-length statistics, i.e. 1D characteristics, have been studied, their geometric properties, particularly fractal properties as self-similarity, and their seasonal variability remain largely unexplored. We identify ISSRs using ERA5 reanalysis data spanning from 2010 to 2020 at three pressure levels. An area-perimeter method is employed to compute fractal dimensions. The results reveal slopes equaling fractal dimensions with high coefficients of determination, strongly suggesting that ISSRs in the UTLS exhibit fractal behavior. A seasonal cycle in both dimension and total count of observed ISSRs was found. We hypothesize that this is caused by the seasonal variation of convective and frontal activity. We further analyzed the latitudinal and longitudinal spans of ISSRs and the path lengths of modeled flights along commercial flight routes. The results of the horizontal extensions are consistent with the fractal properties, and suggest distinct formation processes for ISSRs.

1 Introduction

Ice supersaturated regions (ISSRs) in the upper troposphere and lower stratosphere (UTLS) serve as key environments for the formation and persistence of in situ cirrus clouds. These regions, defined by a relative humidity with respect to ice (RHi) exceeding 100%, occur when the water vapor partial pressure p_v exceeds the water vapor saturation pressure over ice at temperature T:

$$\mathrm{RH_i} = 100\% \cdot \frac{p_v}{p_{si}(T)} = 100\% \cdot S_i, \tag{1}$$

With the saturation ratio S_i. Ice supersaturation - first described by Alfred Wegener (1911) - is a frequent and widespread phenomenon in the UTLS (see, e.g., (Gierens and Spichtinger, 2000; Spichtinger et al., 2003b; Gettelman et al., 2006; Lamquin

https://doi.org/10.5194/egusphere-2025-2498
Preprint. Discussion started: 18 July 2025

et al., 2012; Petzold et al., 2020; Reutter et al., 2020)), where the cold and dry conditions render even small variations in humidity highly significant. ISSRs not only serve as a key environment for the formation of in situ cirrus clouds (Krämer et al., 2016), but also as a prerequisite for persistent contrails (Stuber et al., 2006; Lee et al., 2010, 2021), which is nowadays a major topic in the context of contrail avoidance, since these contrails can persist for over 10 hours and spread into contrail cirrus (Haywood et al., 2009). Cloud free ISSRs themselves have a relatively minor direct influence on the local radiation budget, their transition into cirrus clouds significantly alters radiative forcing (Fusina et al., 2007). ISSRs and cirrus clouds are predominantly found in the upper troposphere, but they can also extend above the tropopause (Spichtinger et al., 2003a; Reutter et al., 2020), affecting the lower stratosphere (LS). The upper troposphere–lower stratosphere (UTLS) region is characterized by extremely cold and dry air masses (Dessler and Sherwood, 2009; Held and Soden, 2000), making outgoing longwave radiation particularly sensitive to absolute changes in UTLS water vapor (Riese et al., 2012). Consequently, variations in ISSR occurrence and cirrus cloud formation within this region have important implications for climate dynamics and radiative balance (Lee et al., 2010). ISSRs are not necessarily cloud free air masses, although former investigations suggest this property. However, the transition from ice clouds to cloud free air is very smooth and usually there are not sharp boundaries. In our study we will not further distinguish between clear and cloudy air, we are just interested in the thermodynamic state of the air masses. While studies have examined the horizontal extent of ISSRs using pathlength statistics (Gierens and Spichtinger, 2000; Diao et al., 2014; Spichtinger and Leschner, 2016; Reutter et al., 2020), their two-dimensional spatial characteristics, including shape and scaling behavior, remain poorly understood and was not studied in detail yet. However, statistical investigations are challenging because of the ISSRs' variability in size and shape, respectively. In addition, some metrics must be defined (or even developed) for studying ISSRs as 2D/3D objects, instead of just using point measurements The radiative effects of cirrus clouds, including those related to natural or anthropogenic origins, are a subject of ongoing research. However, this study emphasizes the structural and statistical properties of ISSRs. Understanding their morphology and variability is essential for improving microphysical parameterizations and for interpreting the atmospheric processes that control cloud evolution in the UTLS.

A potential approach in studying the geometric properties of ISSRs is to examine their potential self-similarity, i.e. the fractal properties of these macroscopic objects. In general, fractals are geometric structures characterized by self-similarity. Self-similar objects exhibit similar patterns on different scales. They differ from traditional Euclidean shapes by possessing non-integer (fractional) dimensions that describe how their complexity changes with scale (cf. Peitgen et al., 2004). Although, the whole research field of fractal geometry was defined by Mandelbrot in 1975, and became famous in the 1980ies (e.g., Mandelbrot, 1982), there were investigations on the fractal nature of natural objects before Mandelbrot. Actually, Richardson carried out first investigations on the nature of turbulence, addressing already some fractal properties (Richardson, 1926). Thus, fractal analysis has a longstanding tradition in atmospheric physics, and especially in cloud physics. In many studies, the fractal nature of clouds is investigated, ranging from cumulus cloud statistics and properties (Cahalan and Joseph, 1989; Joseph and Cahalan, 1990; Cahalan et al., 1994; Gotoh and Fujii, 1998; Siebesma and Jonker, 2000), rain and hail clouds (Lovejoy, 1982; Lovejoy and Mandelbrot, 1985; Rys and Waldvogel, 1986), tropical clouds (Benner and Curry, 1998; Batista-Tomás et al., 2016), noctilucent clouds (von Savigny et al., 2011; Brinkhoff et al., 2015), and cloud fields in high resolution models

https://doi.org/10.5194/egusphere-2025-2498
Preprint. Discussion started: 18 July 2025

(Christensen and Driver, 2021), respectively. In addition, fractal analysis is a key technique for turbulence theories and data evaluation (see, e.g., Sreenivasan and Meneveau, 1986; Sreenivasan, 1991). In some studies, clouds and turbulence investigations are combined in order to explain fractal properties of clouds by the underlying turbulence (or diffusion) characteristics (see, e.g., DeWitt et al., 2024; Rees et al., 2024). However, ISSRs or cirrus clouds were not investigated in this respect. If ISSRs also display self-similar characteristics, determining their fractal dimension can provide insight into their spatial attributes and characteristics. In addition, these properties should be represented in models on different scales; thus, such properties might serve as indication for correct representation of ISSRs and cirrus in model parameterisations.

To identify and study ISSRs, we analyze ERA5 reanalysis data that incorporates absolute humidity, temperature and pressure and distinguish between ice sub- and supersaturated air masses applying a threshold of $S_{i,\mathrm{threshold}} = 0.9$ taking into account the dry bias of ERA5 in the tropopause region (Reutter et al., 2020). As a result a simplified binary representation of these regions is obtained. Applying a definition for connection on gridded data we determine ISSRs as connected areas. Based on this consideration the actual areas and perimeters of ISSRs are calculated to accurately describe their shapes. We take also into account the effects of Earth's curvature and the uneven distribution of grid points. To asses the fractal characteristics of ISSRs, we examine the area-perimeter relation. Plotting the measured area against the perimeter on logarithmic scales shows linear behaviour with slope α, constituting the fractal dimension. This analysis provides us a quantitative measure of the macroscopic objects. This has implications for further investigations. By exploring and quantifying the self-similarity as a fractal characteristic of these regions and assigning them a dimension we may refine atmospheric models and improve representations of high-altitude ISSRs. More accurate geometric characterizations of ISSRs could enhance climate models, improve weather forecasting, and optimize aviation routing to mitigate contrail formation. Enhanced accuracy and precision in our understanding of atmospheric phenomena, coupled with streamlined and efficient computational processes, may lead to improved models for weather forecasting, climate prediction and contrail avoidance.

The study is structured as follows. In Sec. 2 the data set and the methods are introduced. In Sec. 3 the fractal characteristics of ISSRs as found in the data are investigated. This is followed in Sec. 4 by the investigation on the horizontal span of ISSRs. The results are discussed in Sec. 5 and conclusions are drawn in Sec. 6.

2 Data and Methods

In this section we present the data set and describe the methods used for the investigation of the data.

2.1 ERA5

The study utilizes eleven years of ERA5 reanalysis data (Hersbach et al., 2020) covering the period from January 1, 2010, to December 31, 2020 (i.e. full 11 years of data). Data is available at the standard synoptic times each day (0, 6, 12, 18 UTC), resulting in a total of 16,060 datasets for analysis. ERA5 provides data with a horizontal resolution of 0.25 degrees in longitude and latitude, respectively. The area used for the analysis is narrowed down to range from 80 to 30 degrees latitude in the Northern hemisphere in order to exclude the tropics and polar regions. In our investigation we focus on pressure levels of 200

https://doi.org/10.5194/egusphere-2025-2498
Preprint. Discussion started: 18 July 2025

hPa, 250 hPa, and 300 hPa representing the upper troposphere and tropopause region (similarly to the investigation by Lamquin et al., 2012).

2.2 Methods

The first objective in the processing of the data is the identification and localization of ISSRs on the respective pressure levels. The defining order parameter of an ISSR is a saturation ratio S_i that exceeds 1. The saturation ratio S_i is calculated using the specific humidity q, temperature T and pressure p as

$$S_i = \frac{p \cdot q}{\epsilon \cdot p_{si}(T)} = \frac{p_v}{p_{si}(T)} \tag{2}$$

using the ratio of molar masses of water and air, respectively, i.e.

$$\epsilon = \frac{M_v}{M_d} \tag{3}$$

and the saturation vapour pressure over ice p_{si} in the formulation by Murphy and Koop (2005)

$$p_{si} = \exp\left(9.5504 - \frac{5723.265}{T} + 3.53068\log(T) - 0.00728332T\right) \tag{4}$$

which is valid for temperatures $T > 100$ K. Specific humidity and temperature are accessible as variables in ERA5 data for various pressure levels. As such, the pressure p is provided as well.

The identification of ISSRs requires a threshold defining supersaturation; actually, this threshold is given by the thermodynamic equilibrium between vapor and ice, which would be $S_c = 1$. However, since ERA5 data underestimate the humidity in the UTLS region (cf. Köhler et al., 2024; Reutter et al., 2020), we choose a threshold value of $S_c = 0.9$. A data point is assigned to be supersaturated (or belongs to an ISSR) if $S_i \geq S_c = 0.9$. Using this criterion we create for each pressure level a two dimensional binary field with subsaturated data points (index = 0) and data points inside an ISSR (index = 1). After identifying the ISSRs on their respective pressure levels, the binary fields are further processed to be prepared for the measuring processes.

Since we are interested in ISSRs as macroscopic objects consisting of many data points, we have to specify which data points are connected, hence forming an ISSR as an island of points with index = 1 on the respective isobaric surface. In figure 1 two possible definitions of neighborhoods of points on gridded data are shown, originating from investigations with cellular automaton (cf. Chopard and Droz, 1998). In case of a 4-neighborhood (or von Neumann neighborhood), the central pixel has only connection to pixels via the four edges of the point, whereas in case of a 8-neighborhood (or Moore neighborhood) the central pixel is additionally connected to pixels via the diagonals[1]. We decided to use the Moore neighborhood for connecting data points as ISSRs, since it seems to be a more physical measure for connecting pixels. However, the definition of connectivity (or equivalently a certain neighborhood) influences the resulting islands of connected pixels and thus number, perimeter and area of resulting ISSRs. Actually, the 8-neighborhood avoids too small areas, which seems to be plausible for our investigations.

[1] In the description of the used program package, the 4-neighborhood is called 1-connectivity, and the 8-neighborhood is called 2-connectivity. Actually, in literature these terms are not frequently used.

https://doi.org/10.5194/egusphere-2025-2498
Preprint. Discussion started: 18 July 2025

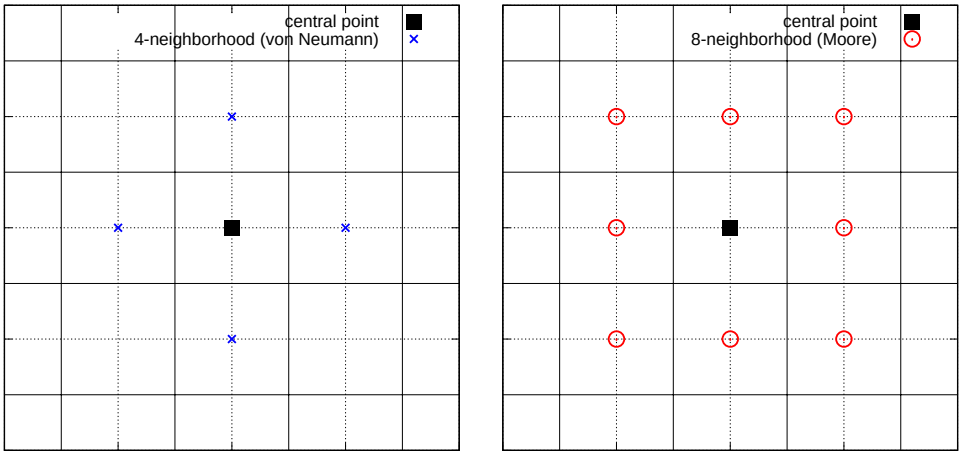

Figure 1. Two possible measures for connecting points on gridded data (cf. Chopard and Droz, 1998). Black square: Center point. Left: Blue crosses indicate points connected to the central point using the 4-neighborhood (von Neumann neighborhood). Right: Red circles indicate points connected to the central point using the 8-neighborhood (Moore neighborhood)

In order to differentiate individual ISSRs and correctly correlate areas and perimeters later, the contiguous binary islands are labeled with non-zero integers counting up from one. Each ISSR is thus allocated a unique number allowing identification by value iteration over ISSRs in the following processes.

In our investigation we concentrate on the midlatitudes in the Northern Hemisphere. However, ISSRs might extend to polar or tropical regions. Thus, we have to specify a criterion for counting ISSRs. All ISSRs crossing the margins of 80 and 30 degrees latitude are deleted (i.e. the index is set to 0) instead of being cut off to avoid skewed results concerning area and perimeter.

2.3 Measuring Island Area

One main challenge in measuring ISSR properties is the distortion caused by the curvature of the Earth and the geographical grid. The distances between neighboring points depends on their position in the grid on a sphere. The area of a pixel decreases with increasing proximity to the pole. In order to assign an area to an ISSR, each pixel needs to be allocated a corresponding area in square meters depending on its position in the geographical grid. The coordinate points themselves are not the vertices of each quadrilateral area but their centers. The data points with coordinates (x, y) being spaced in 0.25 degree intervals results in the vertices $v_1 = (x-0.125, y+0.125)$, $v_2 = (x-0.125, y-0.125)$, $v_3 = (x+0.125, y-0.125)$, $v_4 = (x+0.125, y+0.125)$, as visualized in figure 2.

In pursuance of the assigning of areas for individual pixels, an array with the same dimensions as those of the data arrays is created. The elements of the two dimensional array represent the quadrilateral areas around the coordinate corresponding to the position in the array. Plugging in the coordinates of each data point for x and y the vertices, the real area is calculated

https://doi.org/10.5194/egusphere-2025-2498
Preprint. Discussion started: 18 July 2025

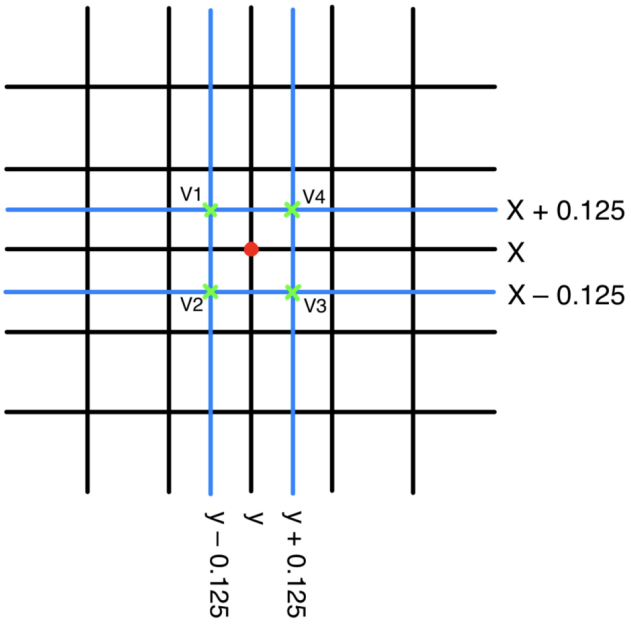

Figure 2. Sketch of calculating the area of a grid point with coordinates (x, y). The area of the grid point is determined by the rectangle defined by vertices $v_1, \ldots, v_4$.

using the Python package `pyproj.Geod` (Snow et al., 2025). Each element in the array of labeled islands has an assigned area in square meters. Iterating over the label values, the areas corresponding to the position of the values are added up. The sum equals the total area of the ISSR.

2.4 Measuring Island Perimeter

Similar challenges as for the determination of one grid point's area are present in measuring the perimeter of ISSRs due to the curvature of the Earth and the grid distortion. Contrary to the areas, the Python tools `pyproj.Geod` for measuring perimeters are not suitable for determining the perimeter of an entire labeled island. The input would have to entail the border pixels only and sort them in a clockwise or anticlockwise direction. The perimeter of holes in the island would not be included. Lastly, the algorithm calculates the perimeter by connecting the pixels center points, which leads to an underestimated perimeter, as depicted in Figure 3.

https://doi.org/10.5194/egusphere-2025-2498
Preprint. Discussion started: 18 July 2025

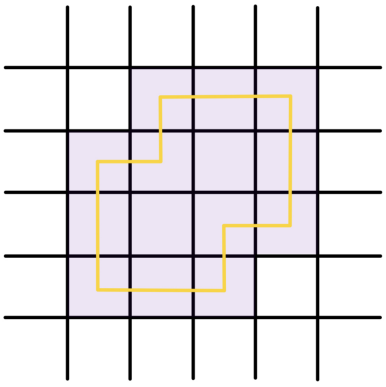

Figure 3. ISSR (purple) and a derived perimeter connecting the pixel centers (orange). This method would underestimate the real perimeter of the object.

This issue was addressed by calculating the real length in meters for each of the four edges of the quadrilateral areas surrounding the data points. Analogous to the process of determining the real areas, an array in the same shape as the data on a pressure level was created. Each element is a list with four elements representing the length of the four sides (figure 4)

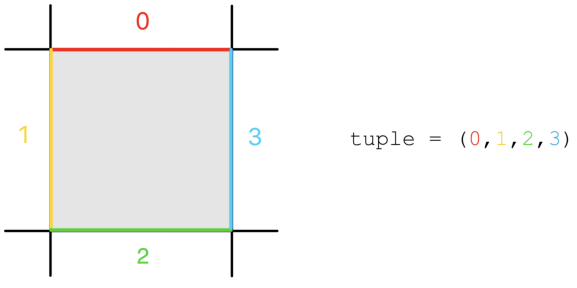

Figure 4. Assigning each perimeter element a place in the tuple. The edge is counted as perimeter, if the neighboring pixel has value = 0.

The perimeter is calculated iterating over the values of the island labels. For each value and island, it is first verified whether a pixel is a border pixel that needs to be considered in the perimeter calculations. The value of each pixel adjacent to one of the four sides is examined to determine if it is zero; in this case a border pixel is found. The corresponding length for the position in the two dimensional array and the side bordering a zero value is added to a perimeter sum. Utilizing this approach enables the measurement of both internal and external borders. One has to mention here that this method leads to a slight overestimation of perimeter values for a gridded object as compared to the analytical manifold. This issue is discussed in appendix **??**.

2.5 Calculation of the Fractal Dimension

The most special property of fractals is self-similarity, which manifests itself in a new approach for the dimension of the objects. The fractal dimension most commonly refers to the Hausdorff dimension, which goes beyond the demands and aims

https://doi.org/10.5194/egusphere-2025-2498
Preprint. Discussion started: 18 July 2025

of this work. The general concept would be to enhance the resolution of the data, i.e. zooming into smaller distances and measuring the length (or even area, volume etc.) using subsequently smaller unit circles, spheres and so on. In the limit of this sequence we obtain the so-called Hausdorff dimension, which is a positive real number $D_H \in \mathbb{R}$ (Peitgen et al., 2004). As a consequence the perimeter of fractal objects become infinity in the limit. Often, this procedure cannot be carried out for real data, also because of the distinct resolution, as in our case of gridded ERA5 data and no possibility to enhance the resolution arbitrarily.

Consequently, a different method is employed to calculate the dimension for data in two-dimension. For this purpose, the area-perimeter relation is investigated. This kind of relationship was introduced by Lovejoy (1982) to study fractal properties of clouds and rain areas. It is defined as follows: we assume that there is a power law relationship between the area A and the perimeter P of a two dimensional object such that

$$A = C \cdot P^{\alpha} \Leftrightarrow \log(A) = \log(C) + \alpha \log(P) \tag{5}$$

Thus, using scatter plots of data points (P, A) in a double logarithmic scale, the area shows a linear behavior with respect to the perimeter with a slope α, which is not necessarily a natural number (i.e. 2 as expected from geometry) but rather a non-negative real number $\alpha \in \mathbb{R}$. For two dimensional objects as ISSRs on a isobaric surface we assume $1 \leq \alpha \leq 2$. The value of α can be determined by linear fit. Note, that our definition is somewhat different to other evaluations (e.g. Batista-Tomás et al., 2016). Often, the perimeter-area relation is defined as $P = \tilde{C} \cdot A^{\frac{D}{2}}$ with the constant D termed as fractal dimension; of course, both exponents can be related by $\alpha = \frac{2}{D}$. Since with Eq. (5) the dimensional relation between length and area, as well as the deviation from the usual dimension, is more obvious, we stay with this definition.

As observed by Cheng (1995), the "dimension" α as derived by the area-perimeter relation does not agree with the Hausdorff dimension in general. This raises the question if the use of this relation and thus the obtained value α is meaningful at all. However, this method is quite frequently employed to ascertain fractal dimensions. Already Mandelbrot et al. (1984) found that the dimension α as obtained by area-perimeter relations agree with fractal dimensions as obtained by spectral analysis. Sakellariou et al. (1991) also discussed this issue, and finally concluded that the method is "the most stable and least ambiguous method" for obtaining fractal dimensions. In Klinkenberg (1994) also other methods for determining fractal dimensions are reviewed. While the dimension α calculated using the area-perimeter relation (Eq. (5)) does not satisfy the mathematical definition of the fractal dimension, it is appropriate to use this approach in order to study the fractal characteristics and properties of phenomena. As these naturally occurring phenomena are not perfect fractals, a pragmatic approach such as the area-perimeter relation is sufficient for a meaningful evaluation.

The area-perimeter relation and variations of it has been used in many applications, as e.g. to study the fractal characteristics of rain and cloud areas (Lovejoy, 1982), to determine the fractal perimeter dimension of noctilucent clouds (von Savigny et al., 2011), to measure the fractal structure of interstellar clouds (Vogelaar and Wakker, 1994), and to classify tropical clouds by their fractal dimension (Batista-Tomás et al., 2016).

For the ERA5 data in this study, the perimeter can not approach infinity as the horizontal resolution limits the frayed nature of the ISSRs perimeter, further justifying the employment of the area-perimeter method. The dimension calculated with the

https://doi.org/10.5194/egusphere-2025-2498
Preprint. Discussion started: 18 July 2025

area-perimeter method will hereafter be referred to as the fractal dimension. As ISSRs have irregular boundaries, the dimension is expected to be in the range $1 < \alpha < 2$. In appendix A we exemplarily show how the fractal dimension might change by either changing the shape of ellipses systematically or fraying the boundary of squares

For gridded data, area and perimeter can only be approximated. Possible errors are underestimation of the area and overestimation of the perimeter, as discussed in Sanchez et al. (2005) and Imre (2006). In appendix B we investigate these issues in case of spheres. However, the analysis makes us confident that the quality of the evaluation is not affected and thus the derived fractal dimensions (i.e. exponents in Eq. (5)) are robust estimates and can be used for further, even quantitative, analysis.

3 Fractal properties of ISSRs

In this section we investigate the fractal properties of ISSRs. In addition, more standard properties, as the number of ISSRs, as well as their seasonal and annual evolution are investigated.

3.1 ISSR Number Count

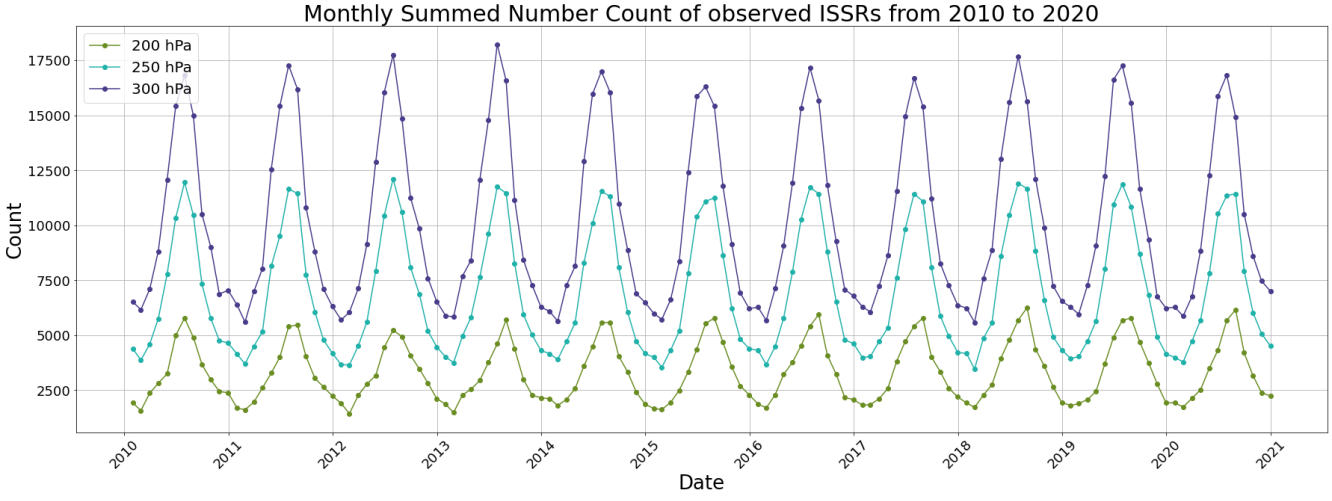

Figure 5. ISSR Number count in each month of the measured from 2010 to 2020 for a pressure level of 200 hPa (green), 250 hPy (cyan) and 300 hPa (purple).

Figure 5 shows number of observed ISSRs by month on the 200 hPa, 250 hPa and 300 hPa pressure levels in the timespan from 2010 to 2020. The total number is a sum of all ISSRs appearing at each point in time. This causes the number to be significantly higher than the ISSRs that appeared in a given month, as ISSRs are counted multiple times when having a lifespan longer that 6 hours. A clear dependence of the number of ISSRs with height is visible. At lower altitudes (i.e. higher pressures) we find much more ISSRs than at higher altitudes. This can be explained by the fact that in the extratropics the (thermal) tropopause is located in the pressure range between 300 and 200 hPa, and ISSRs are almost exclusively located in

https://doi.org/10.5194/egusphere-2025-2498
Preprint. Discussion started: 18 July 2025

the troposphere; only few ISSRs seem to reach into the stratosphere (Spichtinger et al., 2003a). Generally, ISSRs are most frequent close to the tropopause.

Actually, the tropopause also shows a seasonal cycle with high altitudes during summer and lower altitudes during winter, respectively. Nevertheless, the probability to measure dry and warm air in the stratosphere at a certain pressure level in the extratropics is much higher for pressure level $p = 200\,\mathrm{hPa}$, than for $p = 250\,\mathrm{hPa}$ or $p = 300\,\mathrm{hPa}$, respectively. This might explain the strong differences in the amount of ISSRs between the three pressure levels. The strong seasonal cycle in the number of ISSRs is a prominent feature, which is most pronounced at pressure level $p = 300\,\mathrm{hPa}$, i.e. in the upper troposphere. We find maxima in summer and minima in winter for all 3 pressure levels. The month with the highest observed number at pressure level $p = 300\mathrm{hPa}$ is July 2013 with 18230 detected ISSRs, whereas the minimum number at the same pressure level with 5591 can be observed in February 2018. Respectively, the highest number of ISSRs at pressure level $p = 200\mathrm{hPa}$ was recorded in May 2018 with 6257 ISSRs, whereas the minimum was observed in February 2012 with 1434 ISSRs. Here, we see the huge spread in the amount of ISSRs.

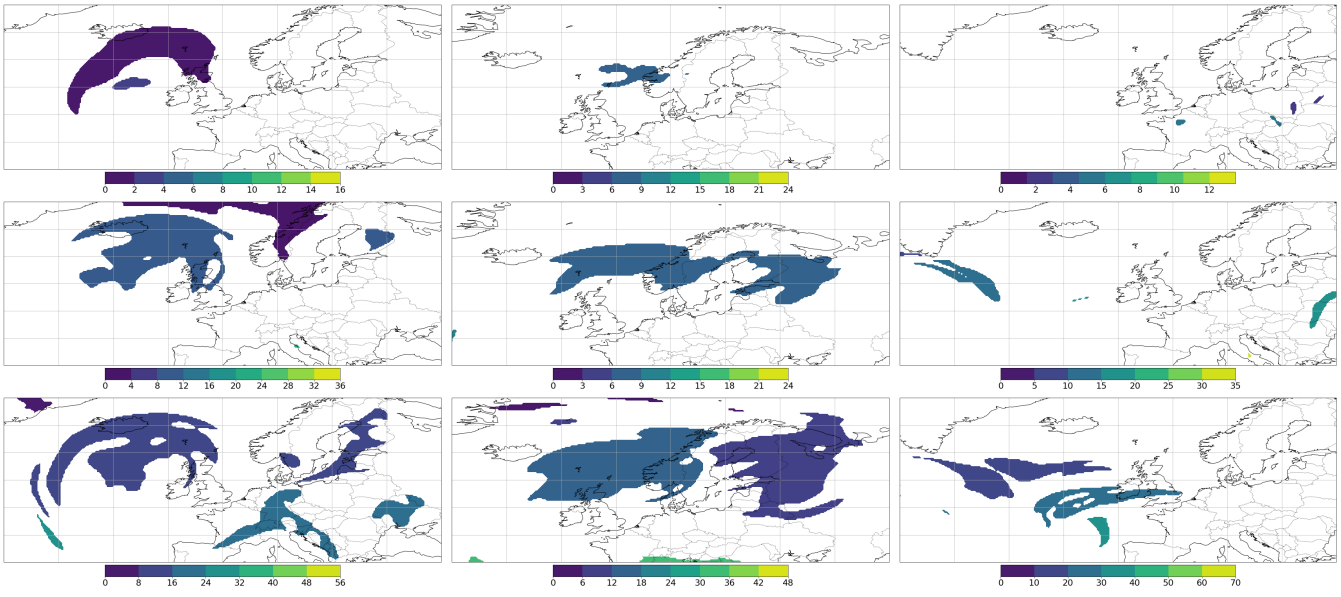

Figure 6. Exemplary ISSRs at pressure levels $p = 200\,\mathrm{hPa}$, $p = 250\,\mathrm{hPa}$, $p = 300\,\mathrm{hPa}$ (top to bottom) at three different times (3 columns) in January 2011. Colors are used to distinguish between individual ISSRs.

In Figure 6 some examples of ISSRs at the three different pressure levels over the North Atlantic region are presented for three times in January 2010, giving a snapshot. A similar example is shown in Figure 7 for one snapshot in July 2019 (3 times). One can clearly see that in winter the ISSRs are more compact and span only a limited area (Fig. 6). At the highest altitudes (i.e. at pressure level $p = 200\mathrm{hPa}$) there are no ISSRs although at lower altitudes (higher pressures) ISSRs can be seen; in winter the tropopause is located at lower altitudes, thus the pressure level $p = 200\mathrm{hPa}$ is (probably) completely contained in the stratosphere. In contrast, in July we find wide spread and quite frayed ISSRs at all three pressure levels (Fig. 7). Even at

https://doi.org/10.5194/egusphere-2025-2498
Preprint. Discussion started: 18 July 2025

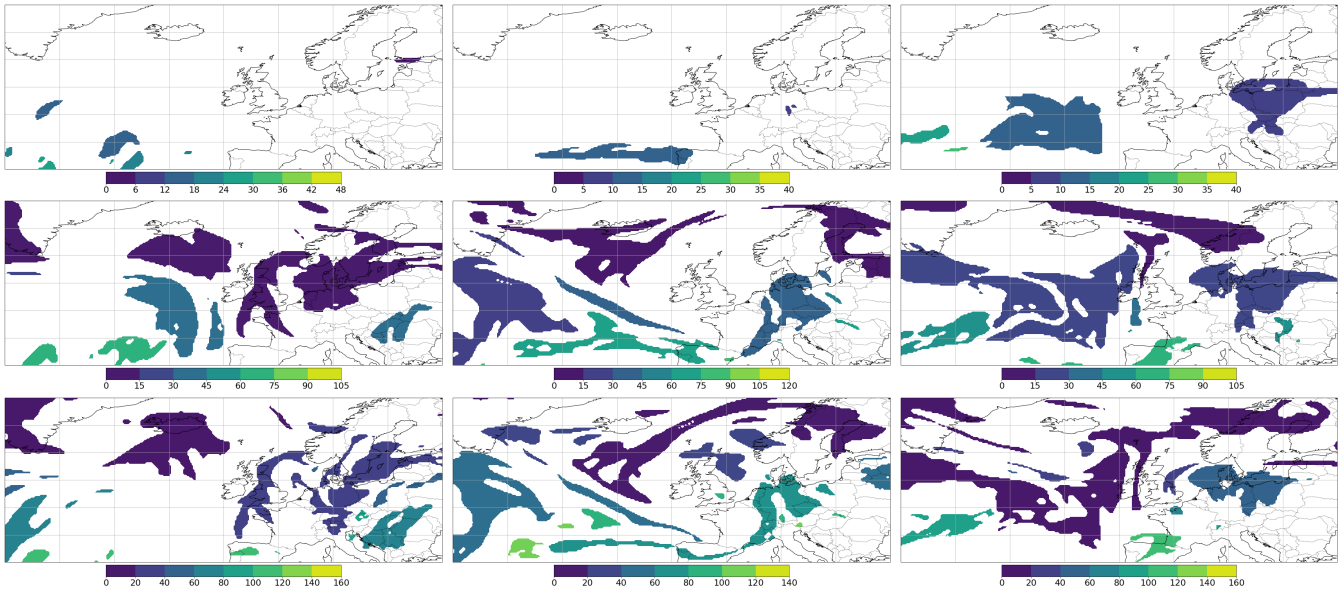

Figure 7. Exemplary ISSRs at pressure levels $p = 200\,\mathrm{hPa}$, $p = 250\,\mathrm{hPa}$, $p = 300\,\mathrm{hPa}$ (top to bottom) at three different times (3 columns) in July 2011. Colors are used to distinguish between individual ISSRs.

$p = 200\mathrm{hPa}$ ISSRs can be found, since during summer the tropopause is located at higher altitudes and ice supersaturation is present there.

The different shape of ISSRs in winter and summer, as observed in Figures 6 and 7, can be also seen in the (statistical) investigations of the fractal dimension, as described in the next section.

3.2 ISSR Dimension

We now determine the fractal dimension for all ISSRs in the data set as derived using the methods explained in section 2.2. We calculate area and perimeter for each detected ISSR (i.e. each connected "island") and determine the fractal dimension by using all data of a certain pressure level for a whole month in a double logarithmic scatter plot. In Figure 8 an example of this procedure is shown for January 2020 (in appendix D another example is provided for July 2020). Three different regimes can be determined in these scatter plots: (a) very small ISSRs with perimeters lower than $\sim 2 \cdot 10^5\mathrm{m}$, (b) an intermediate regime containing most of the ISSRs (representing fractal characteristics), and (c) a regime of very large ISSRs with perimeters larger than $\sim 10^7\mathrm{m}$; for all three regimes we see different signatures of fractal dimensions. However, the procedure of linear regression is applied to the intermediate regime, including most of the detected ISSRs. For this regime we obtain fractal dimension with values $\alpha \sim 1.55 - 1.70$.

The deviation from the regression line of ISSRs with very low perimeters (regime (a)) most probably represents single pixel ISSRs or ISSRs with very few pixels. The minimal amount of pixels limits the degree of irregularity and frayed boarders. Single pixels, which are approximated as rectangles, have dimension $\alpha = 2$ by definition. This steeper slope explains the appearance

https://doi.org/10.5194/egusphere-2025-2498
Preprint. Discussion started: 18 July 2025

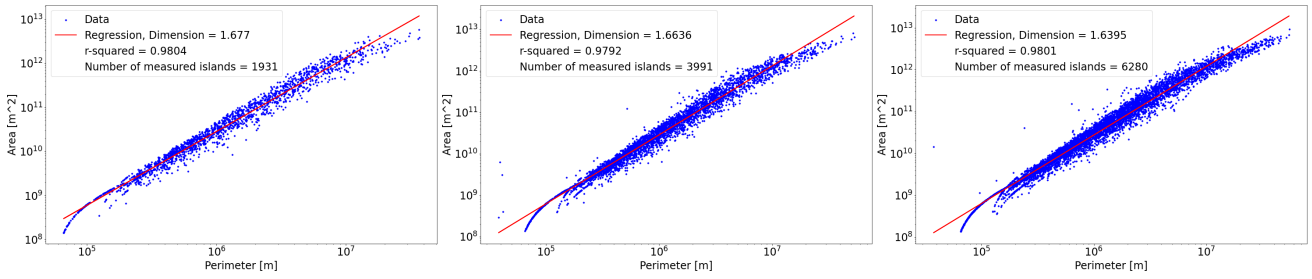

Figure 8. Determination of the fractal dimension via fits to the area-perimeter relation 5 in case of January 2020. Blue dots indicate the data points (tupel (P,A)), red lines are the fits from linear regression. Left: Pressure level $p = 200\mathrm{hPa}$; middle: Pressure level $p = 250\mathrm{hPa}$; right: Pressure level $p = 300\mathrm{hPa}$

of the data points at low perimeters sufficiently well. In the intermediate regime (b), a linear relation is well pronounced with only small scatter around the linear regression line. If we proceed to very large perimeters (regime (c)), there seems to be a kind of scale break at perimeters larger than $\sim 10^7\mathrm{m}$. For these very large ISSRs, we see a kind of bend in the scatter plot, indicating a smaller linear slope, thus implying a smaller fractal dimension. As illustrated in the simple examples presented in appendix A, the reduction of fractal dimension for larger objects might be driven either by more elongated objects (as in case of the ellipses pulled apart) or by more frayed objects. Both reasons seem to be plausible from the presented snapshots in Figs. 6 and 7; however, a clear attribution is not possible.

Finally, we determine the annual evolution of the fractal dimension in regime (b) as obtained from monthly data at different pressure levels; the results are represented in Figure 9. First, we again see a clear separation by vertical levels. For each month the fractal dimensions are ordered such that the highest value is assigned to pressure level $p = 200\mathrm{hPa}$, followed by the medium value at pressure level $p = 250\mathrm{hPa}$ and the lowest value at pressure level $p = 300\mathrm{hPa}$, respectively. The fractal dimensions of the observed ISSRs are in the ranges $\sim 1.61-1.69$ ($p = 200\mathrm{hPa}$), $\sim 1.56-1.66$ ($p = 250\mathrm{hPa}$), and $\sim 1.55-1.64$ ($p = 300\mathrm{hPa}$), respectively. All fractal dimensions show a strong seasonal cycle with minima during summer and maxima during winter seasons, respectively. The amplitude for the cycles is largest for the pressure range $p = 250\mathrm{hPa}$, whereas it is reduced or damped for the other two levels, but it is still well pronounced. The correlation coefficient for the linear fit in the intermediate regime (b) indicating the quality of the fits by the linear regression are quite high ($r^2 \geq 0.95$). Thus, the results are quite robust and constitute a new and pronounced feature of ISSRs.

https://doi.org/10.5194/egusphere-2025-2498
Preprint. Discussion started: 18 July 2025

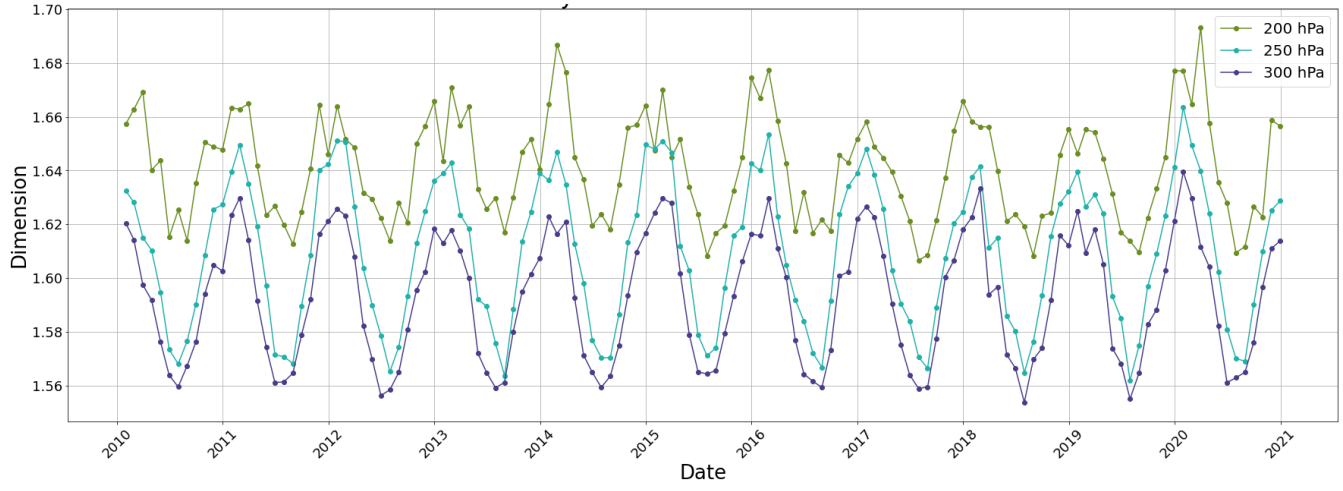

Figure 9. Fractal dimensions at three pressure levels in a monthly resolution for the whole time span of 11 years of ERA5 data.

Although, this study is the first one investigating the fractal nature of ISSRs, we can try to compare our results to similar studies on fractal dimensions, e.g., for high clouds observed in satellite data and models with global storm resolving resolutions. Since ice clouds form in ISSRs, there should be a comparable relationship. Batista-Tomás et al. (2016) evaluated satellite data of (ice) clouds and found a fractal dimension of $\alpha \sim 1.46$ for high cirrus clouds, and a fractal dimension of $\alpha \sim 1.70$ for cumulonimbus clouds. These values are in the same range as values of α found in this study, showing clear fractal properties of clouds. Christensen and Driver (2021) investigated high resolution model data and found fractal dimensions in the range $\alpha \sim 1.33 - 1.5$, which are also comparable to our findings. Note, that the values of the two studies are recalculated using our definition of fractal dimension in the perimeter-area relation in Eq.(5).

4 Horizontal span of ISSRs

Although ISSRs are quasi 2D objects on isobaric surfaces, a common measure for ISSRs is the so-called pathlength. If a (commercial) aircraft crosses an ISSR, the track inside the ISSR is termed as pathlength. Gierens and Spichtinger (2000) first investigated pathlength statistics of ISSRs using data from the MOZAIC project (Marenco et al., 1998), this study was later extended by Spichtinger and Leschner (2016) for IAGOS data (Petzold et al., 2015). The pathlengths, although constituting just 1D tracks through 3D objects give a first idea about the horizontal extension and even the shape of ISSRs. Since we use quasi 2D data (at pressure levels) in this study, we can generate artificial pathlengths in order to simulate the distribution of realistic pathlengths. These can be used in two different ways. First, using zonal and meridional directions (i.e. East-West, North-South), we can statistically investigate the horizontal extension (or span) of ISSRs in a systematic but less realistic way (if one thinks about flight tracks). Second, we can generate realistic pathlengths in using simulated flight tracks along geodesics between frequently used airports. These pathlengths then can be compared to realistic distributions as derived from aircraft data (e.g. from the IAGOS project, see Petzold et al., 2015).

https://doi.org/10.5194/egusphere-2025-2498
Preprint. Discussion started: 18 July 2025

For the determination of longitudinal and latitudinal spans of ISSRs, we proceed as follows. These spans are not measured as a means to obtain the largest extent in one direction, but rather to generate a full set of spans along latitudes/longitudes touched by the respective ISSR. Thus, the ISSR is therefore measured in "slices" with a spacing of 0.25 degrees. This procedure is carried out for both directions, zonal and meridional, respectively. The resulting data is divided by seasons, i.e. spring (MAM), summer (JJA), autumn (SON) and winter (DJF), and is used for deriving statistical distributions of the horizontal extension/spans of ISSRs.

Former investigations of pathlength statistics showed Weibull-type distributions (Gierens and Spichtinger, 2000; Spichtinger and Leschner, 2016). ISSRs are extreme events in some sense, since the majority of data points in the ERA5 data set (and even in other data sets) show values below ice saturation. Just a small amount of regions in the UTLS are in the status of ice supersaturation. The Weibull distribution is one special case of the more general extreme value distribution (see, e.g., Sornette, 2006), thus it is not that surprising to find this type of distributions in our investigation of "extreme events" ISSRs. The probability density function of a Weibull distributed random variable x is given by $f(x) = \gamma p x^{p-1} \exp(-\gamma x^p)$ with shape parameter $p \in \mathbb{R}_+$ and scale parameter $\gamma \in \mathbb{R}$, respectively. The parameter p determines the overall shape of the distribution; it can be obtained by using a Weibull plot (and the cumulative distribution $F(x) = 1 - \exp(-\gamma x^p)$) with linear regression. The slope of the regression line is the parameter p. For more details about Weibull plots we refer to appendix C.

4.1 Span along Longitude

First, we investigate the latitudinal slices, i.e. pathlengths along longitudes in North-South direction. The normalized statistical distributions for the four seasons, differentiated into three pressure levels are shown in Figure 10. Here, we use the full data set for the whole period between 2010 and 2020.

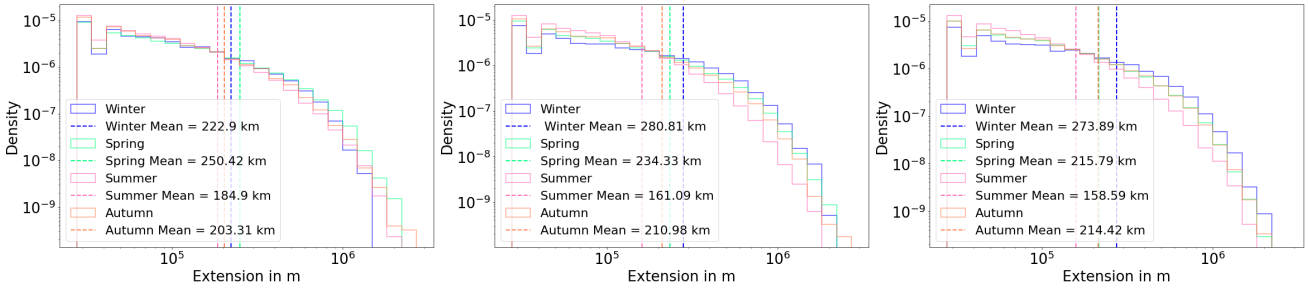

Figure 10. Distributions of pathlengths in North-South directions for different seasons. Left: 200 hPa, middle: 250 hPa, right: 300 hPa

For the pressure pevels $p = 250/300\text{hPa}$, the mean North-South span of ISSRs is significantly higher in winter compared to the summer months, while autumn and spring exhibit minimal disparity. For the lowest pressure level (i.e. highest altitude, $p = 200\text{hPa}$), we find a slightly different behavior, i.e. the maximum mean value occurs for spring season, whereas the minimum remains in summer. While the density does not differ between the seasons for ISSRs up to a size of approximately 10^6m, the disparity between summer and winter gets larger with increasing the measured span. The absolute mean span increases

https://doi.org/10.5194/egusphere-2025-2498
Preprint. Discussion started: 18 July 2025

	DJF	MAM	JJA	SON
200hPa	222.90	250.42	184.90	203.31
250hPa	280.81	234.33	161.09	210.98
300hPa	273.89	215.79	158.59	214.42

Table 1. Mean values of latitudinal span (i.e. pathlengths in North-South direction) statistics (in km).

with decreasing pressure (i.e. with rising altitude levels); the relative difference comparing summer and winter also slightly increases with higher pressure (i.e. lower altitudes). The mean values are reported in Table 1. The strong seasonal cycle is present in both, the mean values and also in the extreme tails of the distributions. For the season with maximum mean values (winter for $p = 250/300\mathrm{hPa}$, spring for $p = 200\mathrm{hPa}$), we find an clearly enhanced probability of finding extremely large pathlengths (i.e. enhanced values in the tail of the distribution), whereas during summer there is a reduced probability of extremely large pathlengths. All histograms show bars representing single pixel and very small ISSRs. The distributions have a strong similarity to Weibull distributions as found in former investigations. Therefore, we use Weibull plots (Figure 11) for further evaluations, i.e. to determine the approximate shape parameter of the distribution.

The data used deliberately does not include measurements shorter than $27\mathrm{km}$, as this is approximately the longest single-pixel length that can be measured in the target region. Including distances below that threshold is not meaningful, since this would introduce artificial biases stemming from different pixel sizes at different locations, leading to artificial breaks of regimes.

The data shows two regimes with roughly linear correlation but different slopes in the Weibull plots (i.e. in the respective values of parameter p). Thus, there are two distinct distributions superimposed in the histograms. The transition between these regimes is roughly located at $\sim 10^5\mathrm{m}$. This alludes to the existences of two different physical formation processes. Neither season nor pressure level influences this observation.

The existence of two clearly separated regions in size points to possibly different formation mechanisms of ISSRs on different scales, i.e. processes acting on distinct but different scales, producing a distinct scale in the horizontal extension of ISSRs. However, this hypothesis is subject of further investigations, since an in depth analysis is out of scope of this study.

The number of points for the 'small regime' is quite small, we only use a linear fit for the regime or larger ISSRs. Here, we can derive the shape parameter p as the slope of the linear fit. We find almost no variation in the shape parameter p, but values in the range $p \sim 1.01 - 1.06$.

4.2 Span along Latitude

Alike investigating the North-South slices along longitudes, we now investigate spans along latitudes, i.e. slices in East-West direction within ISSRs. The normalized statistical distributions for the four seasons, differentiated into three pressure levels are shown in Figure 12. Again, we use the full data set for the whole period between 2010 and 2020.

https://doi.org/10.5194/egusphere-2025-2498
Preprint. Discussion started: 18 July 2025

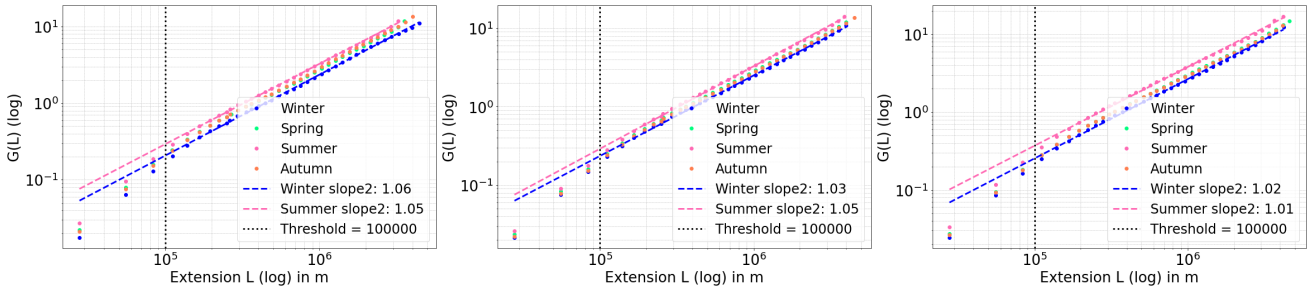

Figure 11. Weibull plots for the pathlength distributions in North-South direction. The linear regression fit is shown for the regime of pathlengths larger than $\sim 10^5$m. Left: 200 hPa, middle: 250 hPa, right: 300 hPa

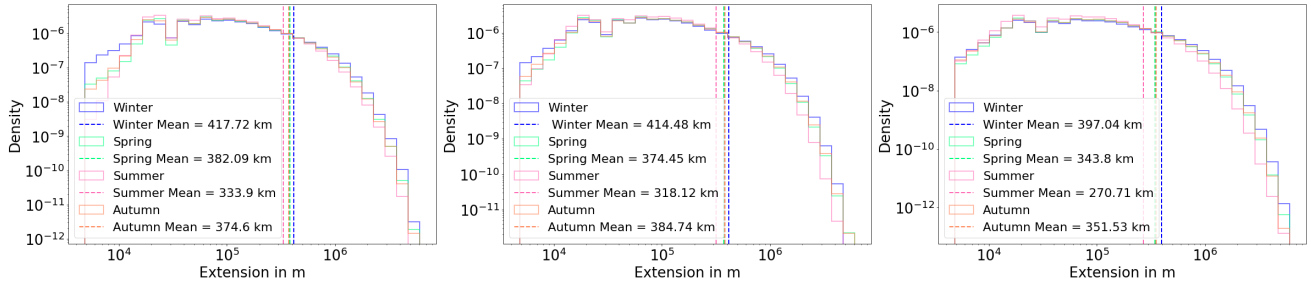

Figure 12. Distributions of pathlengths in East-West directions for different seasons. Left: 200 hPa, middle: 250 hPa, right: 300 hPa

The distribution of measured latitudinal distances shows almost the same qualitative characteristics as the longitudinal counterpart. For all pressure levels, the mean span is significantly higher in the winter months compared to the summer months. Spring and autumn showcase distances between the summer and winter mean and differ only slightly from another. Differences in the distribution of spans by season are most clear for larger spans. The mean generally decreases slightly with a higher pressure level, with only the exception of the autumn mean being higher at $p = 250\text{hPa}$ compared to the level at $p = 200\text{hPa}$. The decrease in mean span with higher pressure is most evident in the summer months. The mean values are reported in Table 2. We also see the same feature of enhanced probability for extremely large pathlengths during winter and reduced probability during summer, respectively.

	DJF	MAM	JJA	SON
200hPa	417.72	382.09	333.90	374.60
250hPa	414.48	374.45	318.12	384.74
300hPa	397.04	343.80	270.71	351.53

Table 2. Mean values of longitudinal (i.e. pathlengths in East-West direction) span statistics (in km)

https://doi.org/10.5194/egusphere-2025-2498
Preprint. Discussion started: 18 July 2025

We again investigate the Weibull plots for the distributions. For the East-West spans it seems that here are three different regimes. A regime of very small pathlengths with no clear Weibull signature, and the two regimes with almost constant but different parameter p as before, separated at values $\sim 10^5$m. The two distinct (Weibull) regimes are more distinguishable compared to the latitudinal data. The regime of very small pathlength might be an artifact of the evaluation. The real area of a pixel (or grid point) depends crucially on the latitude. For East-West spans we regularly scan through at all latitude, thus high latitude circles will systematically produce small horizontal sizes for ISSRs consisting of few pixels.

We derive the shape parameter only for the regime with pathlengths larger than 10^5m. The parameter values only slightly vary, with values $p \sim 1.02 - 1.07$.

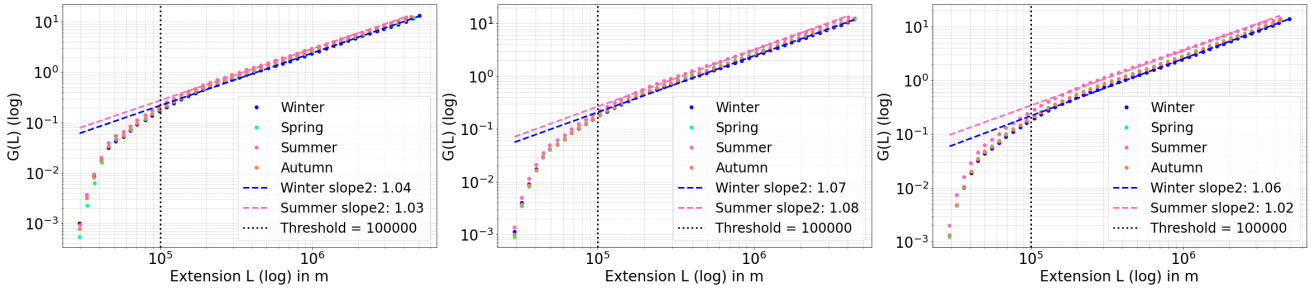

Figure 13. Weibull plots for the pathlength distributions in East-West direction for different seasons. Left: 200 hPa, middle: 250 hPa, right: 300 hPa

4.3 Span along modeled aircraft tracks

In addition to the longitudinal and latitudinal measurements, realistic pathlengths are investigated. In lieu of real in situ measurements, some tracks of commercial aircraft routes are investigated. For this purpose we exemplarily chose four typical flight routes between the US and Europe, based on the flight tracks frequently found in the IAGOS data (Petzold et al., 2015). The four tracks, i.e. direct flight routes are Berlin–Chicago, Frankfurt–Atlanta, London–New York, and Paris–Miami, respectively, placed on the geodesics on a sphere (see Figure 14). The pathlengths are obtained by measuring the distance along the sections of ice supersaturation on the flight track from airport to airport.

https://doi.org/10.5194/egusphere-2025-2498
Preprint. Discussion started: 18 July 2025

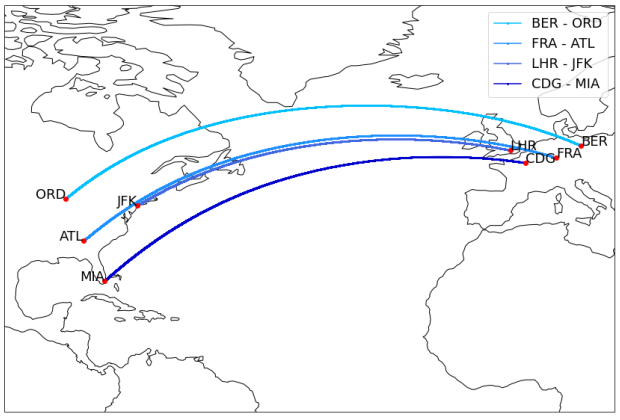

Figure 14. Typical flight routes of commercial air traffic for some important airports in the US (Atlanta, Chicago, Miami, New York) and Europe (Berlin, Frankfurt, London, Paris). These flight routes can be seen in the measurement data from the IAGOS project.

The histograms (Figure 15) show numerical artifacts for small and single pixel ISSRs. However, we find the same features of pathlength statistics for mean values and distributions as before. With the exception of spring at $p = 200\mathrm{hPa}$, the winter months yield the highest mean pathlengths, followed by spring and autumn with similar length and summer with the shortest mean distances. The mean summer pathlength is shorter the higher the pressure. This is only true for the other seasons when comparing values at $p = 250\mathrm{hPa}$ to those at $p = 300\mathrm{hPa}$. The difference in probability is more apparent for larger distances. The mean values of the pathlength distributions are represented in table 3.

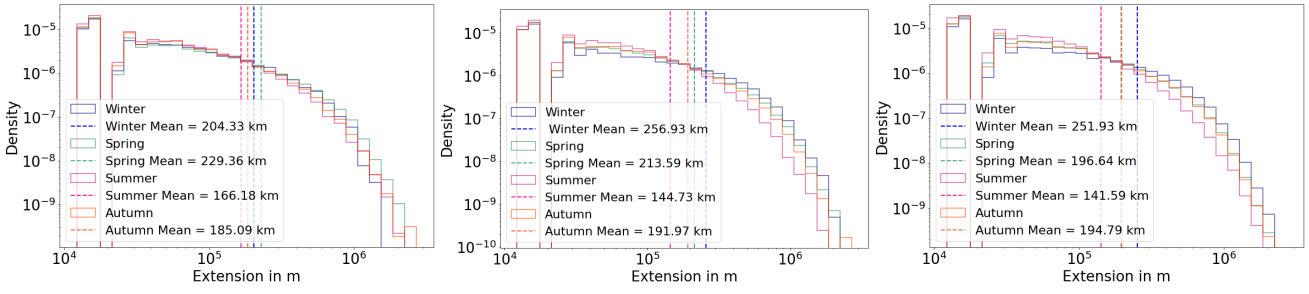

Figure 15. Distributions of realistic pathlengths for different seasons as simulated by assuming common flighttracks (as shown in fig. 14). Left: 200 hPa, middle: 250 hPa, right: 300 hPa

In the evaluation of the Weibull plots, we find again two different regimes of distinct Weibull distributions with different values of p, separated at pathlengths $\sim 10^5\mathrm{m}$, as before. However, the difference in the regimes is more pronounced than in the former evaluations of North-South and East-West extensions. For the large pathlength regime we see a more pronounced seasonal cycle, as clearly represented in the values of Weibull parameter p, thus resulting into distinct changes in the tail of pathlength distribution. For winter season, we find more large pathlengths (i.e. higher values $p \sim 1.07 - 1.112$), whereas in summer less large pathlengths can be found ($p \sim 0.91 - 0.95$).

https://doi.org/10.5194/egusphere-2025-2498
Preprint. Discussion started: 18 July 2025

	DJF	MAM	JJA	SON
200hPa	204.33	229.36	166.18	185.09
250hPa	256.93	213.59	144.73	191.97
300hPa	251.93	196.64	141.59	194.79

Table 3. Mean values of pathlength (i.e. artificial flight tracks) statistics (in km)

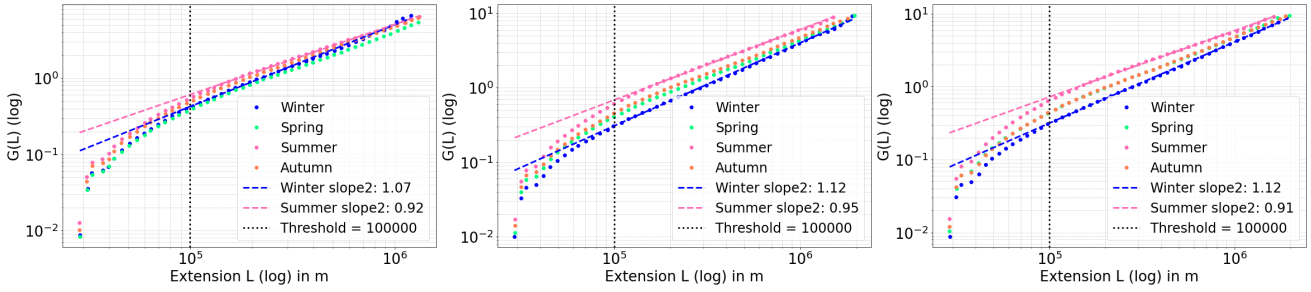

Figure 16. Weibull plots for the pathlength distributions of realistic pathlengths simulated by common flighttracks. Left: 200 hPa, middle: 250 hPa, right: 300 hPa

The mean values as well as the distributions for the artificial pathlengths as obtained from the ERA5 data agree very well with evaluations of pathlengths using IAGOS data (Spichtinger and Leschner, 2016). The distribution also are of Weibull type, however with a clearer scale break and thus well separated regimes. Using a coarsening of the high resolution aircraft data, the mean values are in the same range as in our investigation (mean values $\sim 220 - 280$km).

4.4 Agreement of pathlength distributions

The results of the longitudinal, latitudinal and pathlength measurements agree well with another. The observation of the summer months yielding the shortest and (mostly) winter the longest mean distances holds true across methods. This agreement applies to most results in terms of dependence on pressure level as well. The mean span is generally larger at lower pressures, i.e. higher up in the atmosphere.

The results of the simulated IAGOS flights in winter not completely following this pattern can be explained by both, the smaller amount of measurements compared to observing the whole atmosphere, and the tropopause being below 200 hPa in winter and thus skewing the results. The similarity of the results for latitudinal and longitudinal span speaks for the invariance of shape to zonal and meridional alignment.

The mean values for East-West spans are generally larger than for the North-South extensions and the flight track pathlengths. THis feature is obvious from the example of ISSRs as show in figs.6 and 7. The ISSRs usually extend more in East-West direction, as driven by the mean large scale flow.

https://doi.org/10.5194/egusphere-2025-2498
Preprint. Discussion started: 18 July 2025

Finally, there is agreement in terms of the scale break in the distributions, manifested in the Weibull plots, which point to two possible physical processes forming ISSRs yielding two distributions.

5 Discussion

As described in the sections above, we found several properties of ISSRs in terms of fractal dimensions and horizontal extensions. More precisely, we can summarize the main findings as follows:

1. There is a seasonal cycle in the number of ISSRs. We find many ISSRs for the summer season, but much less in winter. There is also a vertical layering of the amount of ISSRs, with high numbers at lower altitudes, and a decrease in the number for increasing heights.

2. We find two main different regimes for the fractal dimensions in the parameter space of perimeter vs. area. For an intermediate regime with perimeters not larger than $\sim 10^7\mathrm{m}$, we find fractal dimensions in order of $\alpha \sim 1.55 - 1.7$; for the larger regime we find a even smaller values of the fractal dimension. The fractal dimensions also show a clear vertical layering with largest values for high altitudes and lower values for low altitudes, respectively.

3. There is a clear seasonal cycle for the fractal dimensions with smaller values for summer and larger values for winter, respectively.

4. In the evaluation of the horizontal extensions of ISSRs, i.e. deriving pathlength in various ways (artificial East-West and North-South spans vs. realistic flight paths), we also find a seasonal cycle. Generally, we find smaller pathlengths during summer (smaller mean values, less extremes), whereas during winter the pathlengths are generally larger (larger mean value, more really large pathlengths). This feature is robust for all evaluated pressure levels.

5. In the pathlengths statistics, we find different regimes, as indicated by different values of the shape parameter p in the Weibull plots, indicating a superposition of two different Weibull distributions. The scale break can be estimated at $L \sim 10^5\mathrm{m}$.

As we have see from the simple exercise in appendix A about changes in fractal dimensions, more elongated or even strongly frayed objects have smaller fractal dimensions. As indicated by the snapshots in Figs. 6 and 7, in summer the ISSRs might be more elongated and certainly more frayed than in winter. The fractal dimension is smaller for ISSRs in summer, thus we expect more frayed/elongated objects. In turn, these objects lead to smaller pathlengths, since crossing such objects lead to generally smaller cross sections of ice supersaturation. On the other hand, ISSRs in winter have larger fractal dimensions, thus suggesting a more compact shape. This is consistent with the pathlength statistics, since crossing of more compact objects leads to less small pathlengths or even to generally larger cross sections. Thus, the seasonal cycles of fractal dimensions and pathlengths, respectively, are physically consistent.

The strong contrast between fractal properties of ISSRs for different seasons suggest different formation processes. For this we might also take into account the seasonal fluctuation in the number of ISSRs with a peak in summer (in agreement

https://doi.org/10.5194/egusphere-2025-2498
Preprint. Discussion started: 18 July 2025

with Reutter et al., 2020). A possible explanation is the transportation of water vapour into the UTLS by convection during the summer months. A multitude of convection sites causes high ISSR numbers while the winter month are dominated by low pressure areas and frontal systems. The ascending air flow of the warm conveyor belt causes a connected area of supersaturation. This hypotheses is supported by the shorter mean latitudinal and longitudinal spans in summer compared to winter months. Extending this hypothesis to the seasonal variation in the fractal dimension, particularly during the period with the lowest values in summer, provides two possible interpretations. One perspective suggests that convective sites lead to ISSRs with frayed boundaries, resulting in long perimeters compared to the smoother edges of ISSRs caused by frontal activity, i.e. large scale dynamics. An alternative interpretation posits that multiple convective ”bubbles” occurring in close proximity may be collectively labeled as a single ISSR. This would lead to elevated perimeters attributed to their intricate structure and the added internal perimeter created by holes that segregate convective regions.

In addition, the scale break in the Weibull plots of the pathlengths also suggest a possible superposition of two different formation pathways. This can possibly originate in the slopes corresponding to smaller and larger ISSRs. Smaller scale ISSRs form in localized lifting phenomena as e.g. convection. Frontal activity and large scale dynamics create larger areas of supersaturation with respect to ice.

However, an in depth investigation of the formation processes of ISSRs for the full data set is beyond the scope of this study, but is planned as future investigation.

6 Conclusions

Ice supersaturated regions in the UTLS are important potential formwation regions of ice clouds and contrails, respectively. For a better understanding of these regions and thus a meaningful representation in models on different scales and resolutions, we investigated ISSRs in the ERA5 data as "macroscopic" and quasi two dimensional objects on pressure levels in the UTLS. Especially, a potential fractal characteristics is investigated. The analysis of the data with the examination of the area-perimeter relation revealed slopes equaling fractal dimensions, providing strong evidence of ISSRs in the UTLS being self-similar. The order of magnitude of the dimension values is reasonable as a value between 1 and 2 is expected for planar shapes with rough edges. Pathlengths were also investigated statistically, providing results consistent with the fractal properties. A seasonal cycle could be found, showing smaller fractal dimensions during summer in agreement with smaller pathlength, and larger fractal dimensions with larger pathlengths during winter, respectively. The seasonal cycle also points to possible different formation processes, producing different fractal features. We hypothesized formation of ISSRs dominantly by convection during summer, and by large scale dynamics during winter season, corroborated by the distinct features of fractal dimensions, pathlengths, and even number of ISSRs. A scale break of pathlength statistics at about $\sim 10^5\mathrm{m}$ also suggested different formation processes. However, a detailed evaluation of these possible formation pathways is beyond the scope of this study.

The impact and implications of these findings are broad. The level of self similarity across scales can prove helpful in modelling more accurate representations of ISSRs and can thus impact forecasts. Knowing that ISSRs largely keep their characteristics irrespective of their scale can simplify their modelling. The identification of fractal structures enriches scientific

https://doi.org/10.5194/egusphere-2025-2498
Preprint. Discussion started: 18 July 2025

inquiry by providing new tools for analysis, enhancing modelling accuracy, and offering deeper insights into the complexity of natural phenomena. As a more practical aspect of the analysis, the fractal properties of ISSRs must be taken into account for the highly discussed concepts of contrail avoidance. Looking at the examples of frayed ISSRs in Figs. 6 and 7, it seems to be very optimistic that contrail avoidance might work in a meaningful way; the large amount of small ISSRs (or short pathlengths) in connection with the huge fractal objects makes it very difficult to manage efficient contrail avoidance in the Northern hemisphere.

https://doi.org/10.5194/egusphere-2025-2498
Preprint. Discussion started: 18 July 2025

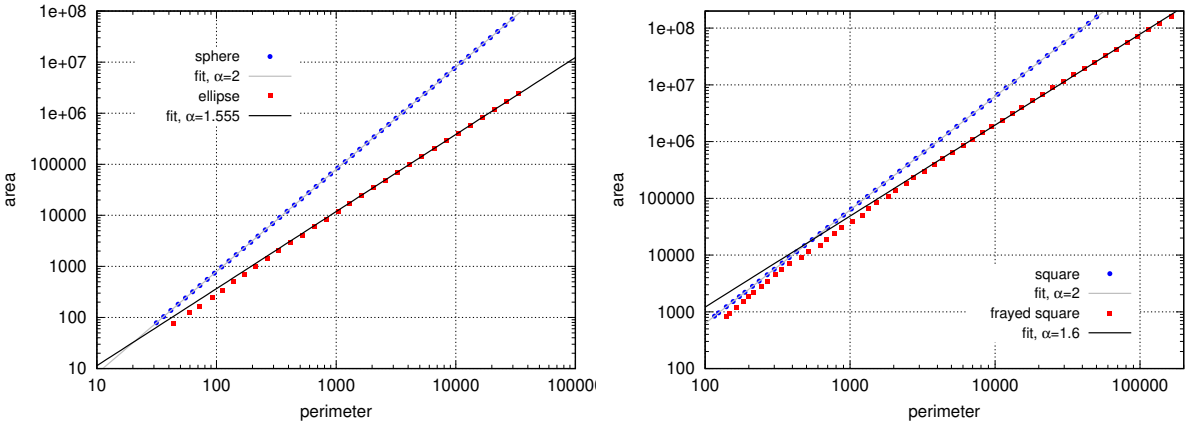

Figure A1. Examples of fractal dimension for 2D objects. Left: sphere vs. consistently stretched ellipse. Right: square vs. frayed square. The fractal dimension is determined using linear regression to the data points in logarithmic scale.

Appendix A: Changes in fractal dimensions

In this appendix we illustrate some effects which might have some influence on the change in the fractal dimension. As a first example, we compare the fractal dimensions of a 2D sphere with a systematically distorted ellipse. For a sphere we can determine the area-perimeter relation analytically, i.e. with $A = \pi r^2$ and $P = 2r\pi$ we obtain $A = C \cdot P^2$ with a constant $C = \frac{1}{4\pi}$ and a "fractal" dimension $\alpha_K = 2$. For our ellipses we prescribe one half axis a and determine the other half axis as $b = a^2$. Using a simple simulation on a 2D rectangular grid we can use a scatter plot of data points to determine the fractal dimension of the ellipse as $\alpha_E \sim 1.52$. Both cases, spheres and ellipses are shown in the left panel of figure A1. Thus, systematically elongated ellipses turn more to a line-shaped geometric object, thus changing the fractal dimension to smaller values.

As a second example, we investigate the case of a square, which boundary is systematically frayed, thus leading to a slightly smaller area but to a strongly enhanced perimeter. Again, for a normal square we would find a fractal dimension of $\alpha_S = 2$. However, for the frayed square, we see that the fractal dimension is also reduced, leading to values of about $\alpha_{FS} \sim 1.6$. The scatter plot of the normal square and the frayed square, respectively, is shown in the right panel of figure A1, together with the linear fits via regression. These two mechanisms can for instance serve for changing fractal dimensions of two dimensional geometric objects.

https://doi.org/10.5194/egusphere-2025-2498
Preprint. Discussion started: 18 July 2025

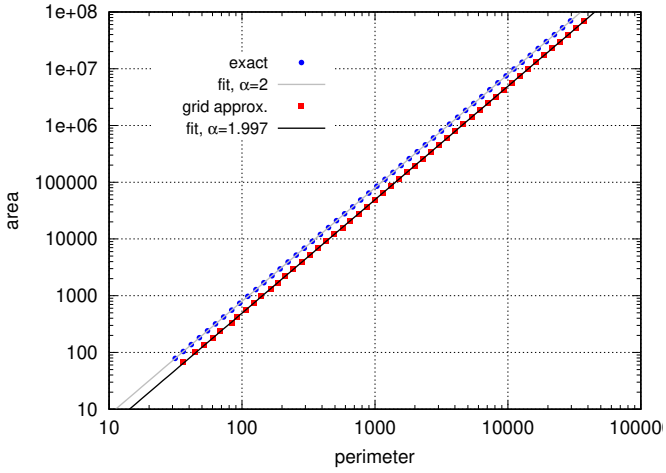

Figure B1. Systematic error for determining perimeters on gridded data.

Appendix B: Potential errors for gridded data: Overestimation of perimeters

It is well known that the calculation of perimeter on gridded data lead to overestimation of this quantity (Imre, 2006). However, it is not completely clear, if and how the area-perimeter relation might change due to this error. Exemplarily, we investigate this for a sphere; we calculate the area and perimeter according to the methods explained above and compare these values with the analytically calculated quantities. The area-perimeter relations are represented in figure B1

Although there is a systematic shift in perimeters, the resulting fractal dimension $\alpha \sim 1.997$ (as a linear fit to the double logarithmic scatter plot) is very close to the analytically determined fractal dimension $\alpha = 2$. Thus, we are quite confident that the systematic overestimation of perimeters does not disturb the quantitative investigations of area-perimeter relations.

Appendix C: Weibull plots

Here we give a short explanation for the use of the Weibull plot. The general form of a Weibull probability distribution of a non-negative random variable x is given by

$$f(x) = \gamma p x^{p-1} \exp(-\gamma x^p) \tag{C1}$$

with the shape parameter $p \in \mathbb{R}_+$, responsible for the slope of the distribution, and the scale parameter $\gamma \in \mathbb{R}$, respectively. The cumulative distribution (i.e. via integration) can be written as

$$F(x) = 1 - \exp(-\gamma x^p), \text{ i.e. } 0 \leq F(x) \leq 1. \tag{C2}$$

https://doi.org/10.5194/egusphere-2025-2498
Preprint. Discussion started: 18 July 2025

This equation can be reformulated as follows.

$$1 - F(x) = \exp(-\gamma x^p) \quad \Leftrightarrow \quad \frac{1}{1-F(x)} = \exp(\gamma x^p) \tag{C3}$$

$$\Leftrightarrow \quad \log\left(\frac{1}{1-F(x)}\right) = \gamma x^p \tag{C4}$$

$$\Leftrightarrow \quad \log\left(\log\left(\frac{1}{1-F(x)}\right)\right) = \log(\gamma x^p) \tag{C5}$$

Finally, we end with this equation

$$\log\left(\log\left(\frac{1}{1-F(x)}\right)\right) = \log(\gamma) + p \cdot \log(x) \tag{C6}$$

thus constituting a linear relationship between the quantities $\eta := \log(-\log(1-F(x)))$ and $\xi = \log(x)$ with a slope of p. Thus, using a scatter plot of variables (ξ, η) we can derive the parameter p via linear regression.

Appendix D: Fractal dimension - additional plots

Here we present the determination of the fractal dimension for three pressure levels in case of July 2020.

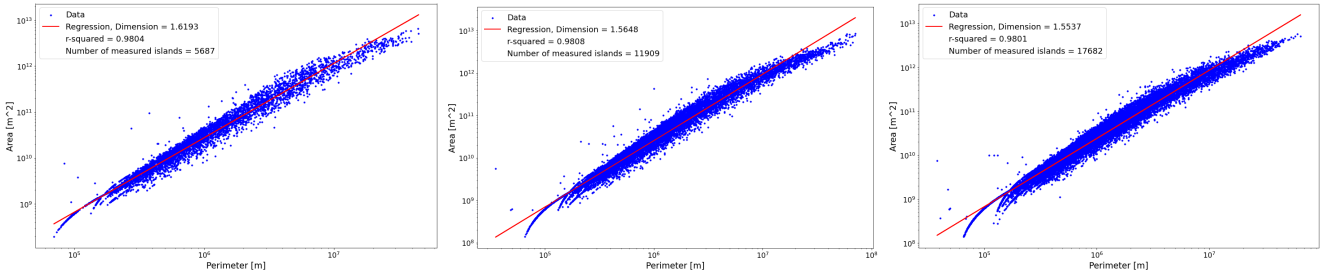

Figure D1. Determination of the fractal dimension via fits to the area-perimeter relation 5 in case of July 2020. Blue dots indicate the data points (tupel (P,A)), red lines are the fits from linear regression. Left: Pressure level $p = 200\text{hPa}$; middle: Pressure level $p = 250\text{hPa}$; right: Pressure level $p = 300\text{hPa}$

https://doi.org/10.5194/egusphere-2025-2498
Preprint. Discussion started: 18 July 2025

Code availability. The code for evaluation is available at Zenodo. DOI: 10.5281/zenodo.15531354

Data availability. The ERA5 data are available at the MARS archive of ECMWF.

Author contributions. HS and PS designed the study. HS and SN developed the data evaluation methods, HS carried out the data analysis. HS, PS and PR discussed the results, and wrote the manuscript.

Competing interests. The authors state that there are no competing interests.

Acknowledgements. Philipp Reutter acknowledges support by the DFG within the Transregional Collaborative Research Centre TRR301 TPChange, Project-ID 428312742 , project C01. Peter Spichtinger acknowledges support by the DFG within the Transregional Collaborative Research Centre TRR301 TPChange, Project-ID 428312742, project B07. The study contributes to the project "Big Data in Atmospheric Physics (BINARY)", funded by the Carl Zeiss Foundation (grant P2018-02-003).

https://doi.org/10.5194/egusphere-2025-2498
Preprint. Discussion started: 18 July 2025

References

Batista-Tomás, A., Díaz, O., Batista-Leyva, A., and Altshuler, E.: Classification and dynamics of tropical clouds by their fractal dimension, Quarterly Journal of the Royal Meteorological Society, 142, 983–988, 2016.

Benner, T. and Curry, J.: Characteristics of small tropical cumulus clouds and their impact on the environment, Journal of Geophysical Research-Atmospheres, 103, 28 753–28 767, https://doi.org/10.1029/98JD02579, 1998.

Brinkhoff, L. A., von Savigny, C., Randall, C. E., and Burrows, J. P.: The fractal perimeter dimension of noctilucent clouds: Sensitivity analysis of the area-perimeter method and results on the seasonal and hemispheric dependence of the fractal dimension, Journal of Atmospheric and Solar-Terrestrial Physics, 127, 66–72, https://doi.org/10.1016/j.jastp.2014.06.005, 2015.

Cahalan, R. and Joseph, J.: Fractal Statistics Of Cloud Fields, Monthly Weather Review, 117, 261–272, https://doi.org/10.1175/1520-0493(1989)117<0261:FSOCF>2.0.CO;2, 1989.

Cahalan, R., Ridgway, W., Wiscombe, W., Bell, T., and Snider, J.: The Albedo of Fractal Stratocumulus Clouds, Journal of the Atmospheric Sciences, 51, 2434–2455, https://doi.org/10.1175/1520-0469(1994)051<2434:TAOFSC>2.0.CO;2, 1994.

Cheng, Q.: The perimeter-area fractal model and its application to geology, Mathematical Geology, 27, 69–82, 1995.

Chopard, B. and Droz, M.: Cellular Automata Modeling of Physical Systems, Collection Alea-Saclay: Monographs and Texts in Statistical Physics, Cambridge University Press, 1998.

Christensen, H. M. and Driver, O. G. A.: The Fractal Nature of Clouds in Global Storm-Resolving Models, Geophysical Research Letters, 48, https://doi.org/10.1029/2021GL095746, 2021.

Dessler, A. E. and Sherwood, S. C.: A matter of humidity, Science, 323, 1020–1021, 2009.

DeWitt, T. D., Garrett, T. J., Rees, K. N., Bois, C., Krueger, S. K., and Ferlay, N.: Climatologically invariant scale invariance seen in distributions of cloud horizontal sizes, Atmospheric Chemistry and Physics, 24, 109–122, https://doi.org/10.5194/acp-24-109-2024, 2024.

Diao, M., Zondlo, M. A., Heymsfield, A. J., Avallone, L. M., Paige, M. E., Beaton, S. P., Campos, T., and Rogers, D. C.: Cloud-scale ice-supersaturated regions spatially correlate with high water vapor heterogeneities, Atmospheric Chemistry and Physics, 14, 2639–2656, https://doi.org/10.5194/acp-14-2639-2014, 2014.

Fusina, F., Spichtinger, P., and Lohmann, U.: Impact of ice supersaturated regions and thin cirrus on radiation in the midlatitudes, Journal of Geophysical Research: Atmospheres, 112, 2007.

Gettelman, A., Fetzer, E. J., Eldering, A., and Irion, F. W.: The Global Distribution of Supersaturation in the Upper Troposphere from the Atmospheric Infrared Sounder, Journal of Climate, 19, 6089 – 6103, https://doi.org/10.1175/JCLI3955.1, 2006.

Gierens, K. and Spichtinger, P.: On the size distribution of ice-supersaturated regions in the upper troposphere and lowermost stratosphere, in: Annales Geophysicae, vol. 18, pp. 499–504, Springer, 2000.

Gotoh, K. and Fujii, Y.: A fractal dimensional analysis on the cloud shape parameters of cumulus over land, Journal of applied meteorology, 37, 1283–1292, 1998.

Haywood, J. M., Allan, R. P., Bornemann, J., Forster, P. M., Francis, P. N., Milton, S., Rädel, G., Rap, A., Shine, K. P., and Thorpe, R.: A case study of the radiative forcing of persistent contrails evolving into contrail-induced cirrus, Journal of Geophysical Research: Atmospheres, 114, 2009.

Held, I. M. and Soden, B. J.: Water vapor feedback and global warming, Annual review of energy and the environment, 25, 441–475, 2000.

Hersbach, H., Bell, B., Berrisford, P., Hirahara, S., Horányi, A., Muñoz-Sabater, J., Nicolas, J., Peubey, C., Radu, R., Schepers, D., Simmons, A., Soci, C., Abdalla, S., Abellan, X., Balsamo, G., Bechtold, P., Biavati, G., Bidlot, J., Bonavita, M., Chiara, G., Dahlgren, P., Dee,

https://doi.org/10.5194/egusphere-2025-2498
Preprint. Discussion started: 18 July 2025

D., Diamantakis, M., Dragani, R., Flemming, J., Forbes, R., Fuentes, M., Geer, A., Haimberger, L., Healy, S., Hogan, R. J., Hólm, E., Janisková, M., Keeley, S., Laloyaux, P., Lopez, P., Lupu, C., Radnoti, G., Rosnay, P., Rozum, I., Vamborg, F., Villaume, S., and Thépaut, J.: The ERA5 global reanalysis, Quarterly Journal of the Royal Meteorological Society, 146, 1999–2049, https://doi.org/10.1002/qj.3803, 2020.

Imre, A.: Artificial fractal dimension obtained by using perimeter-area relationship on digitalized images, Applied Mathematics and Computation, 173, 443–449, https://doi.org/10.1016/j.amc.2005.04.042, 2006.

Joseph, J. and Cahalan, R.: Nearest Neighbor Spacing of Fair Weather Cumulus Clouds, Journal of Applied Meteorology, 29, 793–805, https://doi.org/10.1175/1520-0450(1990)029<0793:NNSOFW>2.0.CO;2, 1990.

Klinkenberg, B.: A review of methods used to determine the fractal dimension of linear features, Mathematical Geology, 26, 23–46, 1994.

Köhler, D., Reutter, P., and Spichtinger, P.: Relative humidity over ice as a key variable for Northern Hemisphere midlatitude tropopause inversion layers, Atmospheric Chemistry and Physics, 24, 10 055–10 072, https://doi.org/10.5194/acp-24-10055-2024, 2024.

Krämer, M., Rolf, C., Luebke, A., Afchine, A., Spelten, N., Costa, A., Meyer, J., Zoeger, M., Smith, J., Herman, R. L., et al.: A microphysics guide to cirrus clouds – Part 1: Cirrus types, Atmospheric Chemistry and Physics, 16, 3463–3483, 2016.

Lamquin, N., Stubenrauch, C. J., Gierens, K., Burkhardt, U., and Smit, H.: A global climatology of upper-tropospheric ice supersaturation occurrence inferred from the Atmospheric Infrared Sounder calibrated by MOZAIC, Atmos. Chem. Phys., 12, 381–405, https://doi.org/10.5194/acp-12-381-2012, 2012.

Lee, D., Pitari, G., Grewe, V., Gierens, K., Penner, J., Petzold, A., Prather, M., Schumann, U., Bais, A., Berntsen, T., Iachetti, D., Lim, L., and Sausen, R.: Transport impacts on atmosphere and climate: Aviation, Atmospheric Environment, 44, 4678–4734, https://doi.org/https://doi.org/10.1016/j.atmosenv.2009.06.005, transport Impacts on Atmosphere and Climate: The ATTICA Assessment Report, 2010.

Lee, D., Fahey, D., Skowron, A., Allen, M., Burkhardt, U., Chen, Q., Doherty, S., Freeman, S., Forster, P., Fuglestvedt, J., Gettelman, A., De León, R., Lim, L., Lund, M., Millar, R., Owen, B., Penner, J., Pitari, G., Prather, M., Sausen, R., and Wilcox, L.: The contribution of global aviation to anthropogenic climate forcing for 2000 to 2018, Atmospheric Environment, 244, 117 834, https://doi.org/https://doi.org/10.1016/j.atmosenv.2020.117834, 2021.

Lovejoy, S.: Area-perimeter relation for rain and cloud areas, Science, 216, 185–187, 1982.

Lovejoy, S. and Mandelbrot, B. B.: Fractal properties of rain, and a fractal model, Tellus A, 37A, 209–232, https://doi.org/10.1111/j.1600-0870.1985.tb00423.x, 1985.

Mandelbrot, B.: The Fractal Geometry of Nature, W. H. Freeman and Co., ISBN 0-7167-1186-9, 1982.

Mandelbrot, B. B., Passoja, D. E., and Paullay, A. J.: Fractal character of fracture surfaces of metals, Nature, 308, 721–722, 1984.

Marenco, A., Thouret, V., Nédélec, P., Smit, H., Helten, M., Kley, D., Karcher, F., Simon, P., Law, K., Pyle, J., et al.: Measurement of ozone and water vapor by Airbus in-service aircraft: The MOZAIC airborne program, An overview, Journal of Geophysical Research: Atmospheres, 103, 25 631–25 642, 1998.

Murphy, D. M. and Koop, T.: Review of the vapour pressures of ice and supercooled water for atmospheric applications, Quarterly Journal of the Royal Meteorological Society, 131, 1539–1565, 2005.

Peitgen, H.-O., Jürgens, H., and Saupe, D.: Chaos and fractals - new frontiers of science (2. ed.)., Springer, ISBN 978-0-387-20229-7, https://doi.org/10.1007/b97624, 2004.

Petzold, A., Thouret, V., Gerbig, C., Zahn, A., Brenninkmeijer, C. A. M., Gallagher, M., Hermann, M., Pontaud, M., Ziereis, H., Boulanger, D., Marshall, J., Nédélec, P., Smit, H. G. J., Friess, U., Flaud, J.-M., Wahner, A., Cammas, J.-P., Volz-Thomas, A., and Team, I.: Global-

https://doi.org/10.5194/egusphere-2025-2498
Preprint. Discussion started: 18 July 2025

scale atmosphere monitoring by in-service aircraft–current achievements and future prospects of the European Research Infrastructure IAGOS, Tellus B: Chemical and Physical Meteorology, 67, 28 452, https://doi.org/10.3402/tellusb.v67.28452, 2015.

Petzold, A., Neis, P., Rütimann, M., Rohs, S., Berkes, F., Smit, H. G. J., Krämer, M., Spelten, N., Spichtinger, P., Nédélec, P., and Wahner, A.: Ice-supersaturated air masses in the northern mid-latitudes from regular in situ observations by passenger aircraft: vertical distribution, seasonality and tropospheric fingerprint, Atmospheric Chemistry and Physics, 20, 8157–8179, https://doi.org/10.5194/acp-20-8157-2020, 2020.

Rees, K. N., Garrett, T. J., DeWitt, T. D., Bois, C., Krueger, S. K., and Riedi, J. C.: A global analysis of the fractal properties of clouds revealing anisotropy of turbulence across scales, Nonlinear Processes in Geophysics, 31, 497–513, https://doi.org/10.5194/npg-31-497-2024, 2024.

Reutter, P., Neis, P., Rohs, S., and Sauvage, B.: Ice supersaturated regions: properties and validation of ERA-Interim reanalysis with IAGOS in situ water vapour measurements, Atmospheric chemistry and physics, 20, 787–804, 2020.

Richardson, L. F.: Atmospheric diffusion shown on a distance-neighbour graph, Proceedings of the Royal Society of London. Series A, Containing Papers of a Mathematical and Physical Character, 110, 709–737, https://doi.org/10.1098/rspa.1926.0043, 1926.

Riese, M., Ploeger, F., Rap, A., Vogel, B., Konopka, P., Dameris, M., and Forster, P.: Impact of uncertainties in atmospheric mixing on simulated UTLS composition and related radiative effects, Journal of Geophysical Research: Atmospheres, 117, 2012.

Rys, F. and Waldvogel, A.: Fractal Shape Of Hail Clouds, Physical Review Letters, 56, 784–787, https://doi.org/10.1103/PhysRevLett.56.784, 1986.

Sakellariou, M., Nakos, B., and Mitsakaki, C.: On the fractal character of rock surfaces, in: International journal of rock mechanics and mining sciences & geomechanics abstracts, vol. 28, pp. 527–533, Pergamon, 1991.

Sanchez, N., Alfaro, E., and Pérez, E.: The fractal dimension of projected clouds, Astrophysical Journal, 625, 849–856, https://doi.org/10.1086/429553, 2005.

Siebesma, A. and Jonker, H.: Anomalous scaling of cumulus cloud boundaries, Physical Review Letters, 85, 214–217, https://doi.org/10.1103/PhysRevLett.85.214, 2000.

Snow, A. D., Whitaker, J., Cochran, M., Miara, I., den Bossche, J. V., Mayo, C., Lucas, G., Cochrane, P., de Kloe, J., Karney, C., Shaw, J. J., Anh, T. Q., Filipe, Ouzounoudis, G., Dearing, J., Lostis, G., Couwenberg, B., Hoese, D., de Bittencourt, H., Little, B., May, R., Itkin, M., McDonald, D., Schneck, C., Gohlke, C., Jurd, B., Raspaud, M., Brett, M., and Meulien, M.: pyproj4/pyproj: 3.7.1 Release, https://doi.org/10.5281/zenodo.14876934, 2025.

Sornette, D.: Critical phenomena in natural sciences: chaos, fractals, selforganization and disorder: concepts and tools, Springer Science & Business Media, 2006.

Spichtinger, P. and Leschner, M.: Horizontal scales of ice-supersaturated regions, Tellus B: Chemical and Physical Meteorology, 68, 29 020, 2016.

Spichtinger, P., Gierens, K., Leiterer, U., and Dier, H.: Ice supersaturation in the tropopause region over Lindenberg, Germany, Meteorologische Zeitschrift, 12, 143–156, https://doi.org/10.1127/0941-2948/2003/0012-0143, 2003a.

Spichtinger, P., Gierens, K., and Read, W.: The global distribution of ice-supersaturated regions as seen by the Microwave Limb Sounder, Quarterly Journal of the Royal Meteorological Society, 129, 3391–3410, 2003b.

Sreenivasan, K.: Fractals And Multifractals In Fluid Turbulence, Annual Review Of Fluid Mechanics, 23, 539+, 1991.

Sreenivasan, K. and Meneveau, C.: The fractal facets of turbulence, Journal of Fluid Mechanics, 173, 357–386, 1986.

https://doi.org/10.5194/egusphere-2025-2498
Preprint. Discussion started: 18 July 2025

Stuber, N., Forster, P., Rädel, G., and Shine, K.: The importance of the diurnal and annual cycle of air traffic for contrail radiative forcing, Nature, 441, 864–867, https://doi.org/10.1038/nature04877, 2006.

Vogelaar, M. and Wakker, B.: Measuring the fratal structure of interstellar clouds, Astronomy and Astrophysics (ISSN 0004-6361), vol. 291, no. 2, p. 557-568, 291, 557–568, 1994.

von Savigny, C., Brinkhoff, L. A., Bailey, S. M., Randall, C. E., and Russell III, J. M.: First determination of the fractal perimeter dimension of noctilucent clouds, Geophysical Research Letters, 38, 2011.